# Stable solar-driven oxidation of water by semiconducting photoanodes protected by transparent catalytic nickel oxide films

Ke Sun[a,b], Fadl H. Saadi[b,c], Michael F. Lichterman[a,b], William G. Hale[b,d], Hsin-Ping Wang[e], Xinghao Zhou[b,c], Noah T. Plymale[a], Stefan T. Omelchenko[b,c], Jr-Hau He[e], Kimberly M. Papadantonakis[a,b], Bruce S. Brunschwig[b,f], and Nathan S. Lewis[a,b,f,g,1]

Divisions of [a]Chemistry and Chemical Engineering and [c]Engineering and Applied Sciences, California Institute of Technology, Pasadena, CA 91125; [b]Joint Center for Artificial Photosynthesis, California Institute of Technology, Pasadena, CA 91125; [d]Department of Chemistry, University of Southampton, Southampton, Hampshire SO17 1BJ, United Kingdom; [e]Computer, Electrical, and Mathematical Sciences and Engineering Division, King Abdullah University of Science & Technology, Thuwal 23955-6900, Saudi Arabia; [f]Beckman Institute Molecular Materials Research Center, California Institute of Technology, Pasadena, CA 91125; and [g]Kavli Nanoscience Institute, California Institute of Technology, Pasadena, CA 91125

Edited by Michael L. Klein, Temple University, Philadelphia, PA, and approved February 10, 2015 (received for review December 3, 2014)

**Reactively sputtered nickel oxide ($NiO_x$) films provide transparent, antireflective, electrically conductive, chemically stable coatings that also are highly active electrocatalysts for the oxidation of water to $O_2$(g). These $NiO_x$ coatings provide protective layers on a variety of technologically important semiconducting photoanodes, including textured crystalline Si passivated by amorphous silicon, crystalline n-type cadmium telluride, and hydrogenated amorphous silicon. Under anodic operation in 1.0 M aqueous potassium hydroxide (pH 14) in the presence of simulated sunlight, the $NiO_x$ films stabilized all of these self-passivating, high-efficiency semiconducting photoelectrodes for >100 h of sustained, quantitative solar-driven oxidation of water to $O_2$(g).**

electrocatalysis | solar-driven water oxidation | photoanode stabilization | nickel oxide

The oxidation of water to $O_2$(g) is a critical process for the sustainable solar-driven generation of fuels, including the generation of carbon-based fuels by the solar-driven reduction of carbon dioxide as well as the generation of $H_2$(g) by solar-driven water splitting (1, 2). Many technologically important semiconductors, including silicon (Si), Group III–V materials such as gallium arsenide (GaAs), and Group II–VI materials such as cadmium telluride (CdTe), have optimal band gaps for use in an integrated, dual light-absorber, solar-fuels generator (3). However, these materials are generally unstable and corrode or passivate rapidly when operated under photoanodic conditions in aqueous electrolytes. Furthermore, the efficient operation of a passive and intrinsically safe water-splitting system requires the use of either strongly alkaline or acidic electrolytes, presenting additional constraints on the stability of the photoanodes and electrocatalysts (4–6).

The search for new, stable compound semiconductors or molecular systems for water oxidation has thus far yielded materials with low efficiencies and/or limited stability (7, 8). An alternative strategy for addressing the lack of materials known to be stable under the conditions needed for the efficient oxidation of water is to protect high-efficiency, technologically important semiconductors to enable their use in integrated solar-fuels generators by using buried semiconductor junctions to form a photovoltaic (PV)-biased electrosynthetic cell (9). In this approach, the surface of the otherwise unstable semiconducting light absorber is covered by a layer of a stable and partially transparent conductive oxide or metal, which serves either as a Schottky barrier or as a transparent conductive contact to a photoelectrode that contains a buried junction to provide the requisite charge separation. Metallized contacts to radial p-n junctions in Si microspheres have been used to effect the unassisted solar-driven splitting of HI(aq) and HBr(aq) (10), and metallized contacts have been used in conjunction with triple-junction–based hydrogenated amorphous Si (*a*-Si:H) photovoltaics for PV-biased electrosynthetic water splitting (11–13). The protective layers used in an integrated photoanode generally require a separate electrocatalyst for the oxidation of water on the electrode surface. Further, the entire assembly must be chemically compatible with and stable in the electrolytes and at the electrode potentials associated with photoelectrochemical water oxidation (14). Metals, metal alloys, semiconductors, degenerately doped transparent conducting oxides, catalytic transition-metal compounds, organic polymers, and surface functionalization methods have all been explored for this purpose, with only limited stability, limited electrical properties at junctions, and/or limited activity for water oxidation observed to date (14).

Sputtered nickel oxide ($NiO_x$) films have been recently shown to be optically transparent, antireflective, conductive, stable, and highly catalytically active while protecting n-Si and $np^+$-Si photoanodes in contact with aqueous 1.0-M KOH for the photoelectrochemical oxidation of water (15, 16). For $np^+$-Si photoanodes, such an approach allowed for the stable production of $O_2$(g) for >1,200 h of continuous operation under 1-Sun simulated solar illumination, with a photocurrent-onset potential of −180 mV relative to the equilibrium water-oxidation potential and current densities in

## Significance

**The development of efficient artificial photosynthetic systems, designed to store solar energy in chemical bonds, requires the pairing of stable light-absorbing electrodes for both the oxidative and reductive half-reactions. The development of such systems has been hindered in part by the lack of semiconducting photoanodes that are stable under the conditions required for the production of $O_2$(g) from water. We demonstrate herein that a reactively sputtered $NiO_x$ layer provides a transparent, antireflective, conductive, chemically stable, inherently catalytic coating that stabilizes many efficient and technologically important semiconducting photoanodes under viable system operating conditions, thereby allowing the use of these materials in an integrated system for the sustainable, direct production of fuels from sunlight.**

Author contributions: K.S. and N.S.L. designed research; K.S., F.H.S., M.F.L., W.G.H., H.-P.W., X.Z., N.T.P., and S.T.O. performed research; K.S., B.S.B., and N.S.L. analyzed data; and K.S., J.-H.H., K.M.P., B.S.B., and N.S.L. wrote the paper.

The authors declare no conflict of interest.

This article is a PNAS Direct Submission.

[1]To whom correspondence should be addressed. Email: nslewis@caltech.edu.

This article contains supporting information online at www.pnas.org/lookup/suppl/doi:10.1073/pnas.1423034112/-/DCSupplemental.

excess of 29 mA·cm$^{-2}$ at the equilibrium water-oxidation potential. We demonstrate herein that this protection strategy can be extended to semiconducting materials used in commercial photovoltaic solar cells and in high-efficiency devices, specifically textured crystalline Si passivated with a layer of amorphous Si, known as a heterojunction Si (HTJ-Si) device with a typical structure of ($p^+$-*a*-Si|i-*a*-Si|n-c-Si|i-*a*-Si|$n^+$-*a*-Si); n-i hydrogenated amorphous Si (*a*-Si:H) structures; and single-crystalline n-type CdTe light absorbers. All of these materials have band gaps appropriate (1–2 eV) for use in integrated solar fuel-generation devices, and this work demonstrates that the $NiO_x$ protection strategy is effective on both single-crystalline and noncrystalline semiconductors.

## Results

Fig. 1*A* shows the effect of the oxygen concentration (0–33.3%) present during the sputter-deposition process on the electrochemical behavior of $NiO_x$ films deposited onto $p^+$-Si substrates ($p^+$-Si|$NiO_x$). The $NiO_x$ films were deposited from a Ni target onto substrates via reactive radio-frequency (RF) sputtering in a high-vacuum magnetron sputtering system with a maximum base pressure of $8 \times 10^{-8}$ Torr (*SI Appendix*, *Text S1*, provides a detailed description of materials and methods). To minimize effects due to electrochemical kinetic overpotentials, the behavior of the film-coated anode was evaluated in contact with $Fe(CN)_6^{4-/3-}$(aq), an electrochemically reversible, one-electron redox couple [0.35 M $K_4Fe(CN)_6$/0.05 M $K_3Fe(CN)_6$ in 1.0 M KCl(aq)]. Increases in the oxygen concentration during sputtering produced more resistive films, as indicated by decreases in the slopes of the linear portions of the current-density vs. potential

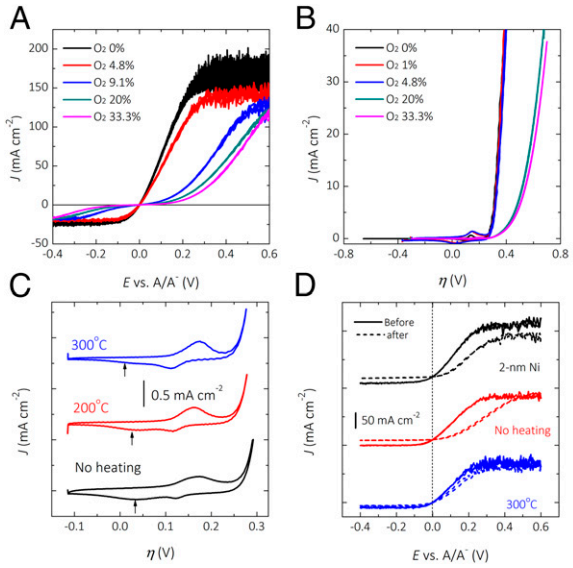


**Fig. 1.** (*A* and *B*) Effect of oxygen concentration during sputter deposition on the conductivity (*A*) and the catalytic activity (*B*) of the resulting activated $NiO_x$ films for the oxidation of water to $O_2$(g), with the overpotential measured relative to the equilibrium water-oxidation potential ($E^{o\prime}(O_2/H_2O)$). (*C*) Effect of deposition temperature on the development of the cathodic double-current peak. (*D*) Effect of deposition temperature on the conductivity of the resulting films before (red and blue solid curves) and after (red and blue dashed curves) activation in 1.0 M KOH(aq) under 4.8% oxygen concentration during sputtering and compared with a 2-nm metallic Ni film (black solid and dashed curves). The conductivity of the $NiO_x$ films (*A* and *D*) was evaluated in contact with an aqueous solution of 0.35 M $Fe(CN)_6^{3-}$/0.050 M $Fe(CN)_6^{4-}$ in 1.0 M KCl as supporting electrolyte. The catalytic activity (*B* and *C*) was evaluated following activation by 10 consecutive cyclic voltammetry scans between 0.93 V and 1.93 V vs. the reversible hydrogen electrode (RHE), without correcting for cell resistance.

(*J*–*E*) data near zero current density, which could be due to the increased oxidation of the Si substrate or to the decreased Ni(II) to Ni(III) ratio in the films, as evidenced by X-ray photoelectron spectroscopy (XPS) (*SI Appendix*, Fig. S2*A*).

Fig. 1*B* shows the effect of the oxygen concentration during sputter deposition on the catalytic activity of the resulting $NiO_x$ films for the oxidation of water to $O_2$(g) in 1.0 M KOH(aq). The behavior depicted in Fig. 1*B* was observed after activation of the film by 10 consecutive cyclic voltammetric scans between 0.93 V and 1.93 V vs. the reversible hydrogen electrode (RHE), without correction of resistance. Increases in the concentration of oxygen during sputtering produced increases in the Tafel slope as well as increases in the catalytic overpotential ($\eta$) for water oxidation (*SI Appendix*, Fig. S1 and Table S1). Over the range of current densities investigated, the catalytic activity for water oxidation of sputtered $NiO_x$ films prepared using an oxygen concentration ≤4.8% was in close accord with that observed for the oxide/hydroxide derived from the oxidation of Ni metal (black curve in Fig. 1*B*). Hence, these films exhibited an overpotential of 330 ± 7 mV to produce an anodic current density of 10 mA·cm$^{-2}$ for water oxidation, within 70 mV of the lowest overpotentials reported to date for water oxidation under these conditions (17), with the other systems generally composed of porous electrocatalyst films that have undesirably high optical absorption and reflection properties. Consistently, no metallic Ni was detected by XPS on sputtered $NiO_x$ films, even on films prepared with oxygen concentrations of only 1% during sputtering (red curve in *SI Appendix*, Fig. S2*A*), and $Ni^0$ was detectable by XPS only for films prepared in the absence of oxygen (black curve in *SI Appendix*, Fig. S2*A*). On the surface of KOH-treated $NiO_x$ and Ni metal films, a trace amount of Fe was observed (*SI Appendix*, Fig. S3), which could contribute to the improvement in the catalytic activity (18–21), although other activation mechanisms such as incorporation of other impurities, thickening of the $Ni(OH)_2$/NiOOH layers, and changes to the crystallinity of the surface (22) could not be excluded. Because the activation process was unchanged for the different samples, the observed differences in *J*-*E* behavior were attributed to the differences in the oxygen concentration during sputter deposition of the films.

Fig. 1*C* shows the effect of the deposition temperature on the *J*-*E* behavior of the Ni redox peak region (overpotential range −0.1 V to ∼0.3 V) after 10 cycles of activation scans in 1.0 M KOH(aq). The cathodic peaks at an overpotential of 0.12 V corresponded to the β-NiOOH/β-$Ni(OH)_2$ transition in lower oxidation states, which increased and became sharper as the deposition temperature increased (20, 23, 24). Moreover, the small reduction peak at an overpotential of 0.036 V developed during the activation of $NiO_x$ and metallic Ni films prepared without substrate heating, which corresponded to the γ-NiOOH/α-$Ni(OH)_2$ transition (25) (highlighted by black arrows in Fig. 1*C*). These observations suggest that substrate heating reduced or delayed the formation of the disordered α-$Ni(OH)_2$/γ-NiOOH catalyst surface phases associated with the development of porosity, presumably through a direct transition between highly crystalline NiO sintered at higher temperatures and surficial NiOOH (23, 26).

Fig. 1*D* shows the electrochemical behavior in $Fe(CN)_6^{3-/4-}$(aq) of $p^+$-Si|$NiO_x$ anodes before (solid curves) and after (dashed curves) activation in 1.0 M KOH(aq). When the substrate was heated during sputter deposition of the $NiO_x$ film, no significant change of conductivity, as measured by the *J*-*E* behavior, was observed after activation (blue curves); whereas samples deposited without heating of the substrate showed a pronounced change in *J*-*E* behavior after activation, with a reduced slope at positive bias and a decrease in the current density at negative bias (red curves). Moreover, a similarly pronounced change in the *J*-*E* behavior was observed on a $p^+$-Si electrode coated with Ni metal (∼2 nm, black

curves). For samples prepared at 300 °C, the Ni(II) peaks observed in the XPS data were more pronounced both before and after activation in KOH than the Ni(II) peaks observed on samples coated with nonannealed $NiO_x$ or metallic Ni (*SI Appendix*, Fig. S2*B*). Both electrically insulating $Ni(OH)_2$ and n-type electrically conductive NiOOH remained on the surface after activation (27) and their concentration is likely dependent on the substrate-heating temperature and on the crystallinity of the starting oxide (*SI Appendix*, Fig. S2*C*). Hence, high deposition temperatures produced $NiO_x$ coatings that were more inert to the physical (Fig. 1*C*) and chemical (*SI Appendix*, Fig. S2*B*) changes caused by anodic activation, which thus affected the energy barriers for hole and electron transfer in electrolytes that contained kinetically rapid one-electron redox species (Fig. 1*D*).

The optical properties of sputtered $NiO_x$ films on polished single-crystalline Si substrates were measured using variable-angle spectroscopic ellipsometry (28) (*SI Appendix*, *Text S2*, provides a detailed description of characterization methods). Fig. 2 *A* and *B* show the measured and fitted ellipsometric and spectrophotometric data for 75-nm-thick $NiO_x$ films coated on $p^+$-Si, with the ellipsometric data obtained using angles of incidence of 65°, 75°, and 85°, respectively. The optical dispersion of the layer derived from a multilayer model exhibited behavior expected for a dielectric oxide, and neither the refractive index ($n$) nor the extinction coefficient ($k$) displayed behavior consistent with Ni metal (increased $n$ and $k$ with a reduced photon energy), consistent with the X-ray photoelectron spectroscopy (XPS) and X-ray diffraction (XRD) analysis (*SI Appendix*, Fig. S2 *A* and *C*). The film exhibited a direction-dependent refractive index ($x$ is in-plane and $z$ is normal to the film surface) as well as a graded index along the z direction (Fig. 2*C*). The extinction coefficient, $k$, was near zero for 1.0 eV < $h\nu$ < 3.5 eV, where the nonzero value of $k$ at $h\nu$ > 3.5 eV was likely due to electron interband excitation in the oxide. The increase in $k$ at $h\nu$ < 1.5 eV

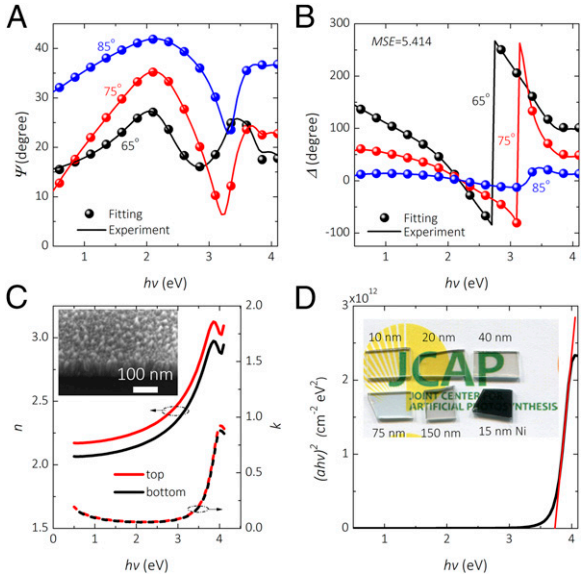


**Fig. 2.** (*A* and *B*) Representative ellipsometric data (curves) and fits (circles) showing the change in polarization as light reflects from a 75-nm $NiO_x$-coated crystalline Si substrate including the amplitude ratio, Ψ (*A*) and the phase difference, Δ (*B*) vs. incident photon energy. (*C*) Graded indexes of the $NiO_x$ films in the $z$ direction. *Inset* displays a cross-sectional SEM image obtained at a 45° tilt angle showing the columnar structure of the sputtered $NiO_x$ film. (*D*) Tauc plot based on the absorption coefficient calculated from the measured extinction coefficient ($k$). *Inset* displays optical images of $NiO_x$ films with various thicknesses and of 15-nm metallic Ni on quartz substrates.

can be ascribed to the free-carrier absorption typically existing in transparent conducting oxides (29), consistent with the presence of a highly conductive film (similar conductivity to metallic Ni shown in Fig. 1*D*) having a large (~$10^{19}$ $cm^{-3}$) free-carrier concentration (15). However, unlike the refractive index, the extinction coefficient, $k$, did not show a strong direction dependence or grading along the $z$ direction. These observations are in accord with the cross-sectional data obtained using scanning-electron microscopy (SEM) (Fig. 2*C*, *Inset*), which showed a columnar structure typically associated with the presence of lower refractive indexes at the bottom of the film due to the nucleation, competitive growth, and coalescence processes. These processes contributed to a continuous change of morphology and texture as a function of thickness (30). Therefore, the columnar structure is consistently associated with the primary origin of the anisotropy in both the refractive index and the electrical conductivity of the films.

Fig. 2*D* shows a Tauc plot [$h\nu$ vs. $(ah\nu)^2$] for $NiO_x$ calculated based on the extinction coefficient, $k$, using the relationship $\alpha = 4\pi k/\lambda$. The direct optical band gap of 3.74 eV was consistent with the data obtained from the Tauc plot derived from the previously reported optical transmission measurements (15).

Metallic electrocatalysts absorb and/or reflect sunlight. Hence, the use of such electrocatalysts in an integrated photoanode involves a trade-off between increasing the film thickness to increase the catalytic activity and decreasing the film thickness to achieve high optical transparency and low reflectance (31). Planar light absorbers without surface texturing are typically reflective, and the dielectric properties of transparent catalyst thin films can therefore be used to minimize these reflections. These optical and ellipsometric results indicate that nearly ideal quarter-wavelength antireflective (AR) behavior can be obtained by integration of a single $NiO_x$ layer with Si, CdTe, and $a$-Si. A calculation based on effective-medium theory showed that coating these semiconductors with a 75-nm-thick layer of $NiO_x$ would result in an effective suppression of reflection at the air–semiconductor interface due to the high refractive indexes of these semiconductors, especially in the visible wavelength region even with water as the incident medium (*SI Appendix*, Fig. S4). Therefore, a thickness of 75 nm was chosen for $NiO_x$ to optimize the antireflection properties in air as opposed to optimizing the electrical conductivity along the direction of the film thickness, the electrocatalytic activity, the number of surface activation sites, or the electrochemical stability of the electrocatalyst, because these latter four properties were unaffected by changes in the film thickness within the range of 10–150 nm (*SI Appendix*, Fig. S5).

Most electrocatalysts of the oxygen-evolution reaction (OER), including transition metals such as Cr, Mn, Fe, Co, Ni, and Ir, as well as their oxides and mixed oxides thereof, are electrochromic (32). The electrochromism results in a change in the optical absorption (effective extinction coefficient) under positive bias in aqueous, especially alkaline, media due to surface adsorption of ions (33). $NiO_x$ films prepared at high temperature exhibited negligible electrochromism (15), in accord with previous results in which high-temperature processing was found to suppress the electrochromic darkening (34, 35). We note that the antireflective performance of $NiO_x$ coatings in water could be further optimized by consideration of the changes in the layered structure of the electrode under anodic conditions. Under anodic conditions, the effective refractive index is reduced due to the presence of electrochemically formed NiOOH (36, 37). This compensation is further supported by the high light-limited current density as well as the high external quantum yield of such electrodes (see below).

Although a 75-nm layer of $NiO_x$ on polished crystalline Si substrates is an effective antireflective coating (*SI Appendix*, Fig. S4), a single material without a properly graded refractive index is not capable of producing broadband antireflection (14)

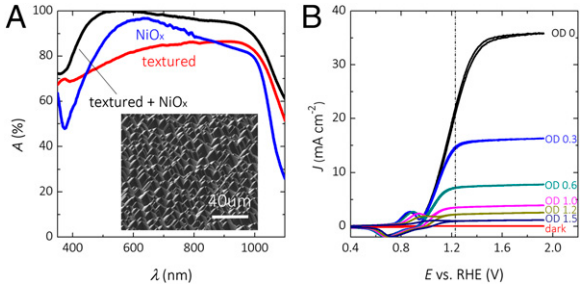


**Fig. 3.** (*A*) Optical absorptance of a textured HTJ-Si device without (red curve) and with (black curve) a 75-nm $NiO_x$ coating compared with a $NiO_x$-coated planar crystalline Si photoelectrode without textures (blue curve). *Inset* displays an SEM image of the textured HTJ-Si surface without $NiO_x$. (*B*) *J-E* data for a HTJ-Si|$NiO_x$ photoanode in contact with 1.0 M KOH(aq) under 100 mW·cm$^{-2}$ of simulated AM 1.5 illumination attenuated by various neutral density filters with different optical densities (OD) and in the dark. The dashed line indicates the equilibrium water-oxidation potential, $E^{o\prime}(O_2/H_2O)$.

(Fig. 3*A*, blue curve). Hence, random surface textures with a smooth transition from ambient to high-index substrates are normally required for reduced sensitivity to the incident wavelength as well as to the angle of incidence. The textured surface of the HTJ-Si cell (Fig. 3*A*, red curve) reduced the reflectance and thus improved the absorptance from ∼60% for a planar crystalline substrate to ∼80% for the textured sample (15). Addition of the $NiO_x$ layer to the textured Si surface reduced the reflectance to below 10%, with nearly 100% absorptance at 550 nm (Fig. 3*A*, black curve). For comparison, a HTJ-Si cell coated with a 2-nm-thick metallic Ni electrocatalyst film (*SI Appendix*, Fig. S6*A*, black curve) exhibited an optical absorptance of ∼70% that was decreased relative to that of a bare HTJ-Si cell (*SI Appendix*, Fig. S6*A*, red curve), due to the higher reflection of this structure.

Fig. 3*B* depicts the *J-E* behavior of a $NiO_x$-coated HTJ-Si photoanode (HTJ-Si|$NiO_x$) in the presence and absence of illumination, respectively. Under 100 mW·cm$^{-2}$ of simulated air mass (AM) 1.5-G illumination, the HTJ-Si|$NiO_x$/1.0 M KOH(aq) contact produced photocurrent-onset potentials of −280 ± 16 mV relative to the equilibrium water-oxidation potential, $E^{o\prime}(O_2/H_2O)$, along with current densities at $E^{o\prime}(O_2/H_2O)$ of 20.7 ± 5 mA·cm$^{-2}$, and a solar-to-$O_2$(g) ideal regenerative cell efficiency of 1.45 ± 0.17%. A load-line analysis using an equivalent-circuit model consisting of a photodiode connected in series with a dark electrolysis cell indicated that obtaining shifts in the *J-E* properties equivalent to those observed for the champion HTJ-Si|$NiO_x$ photoanode in 1.0 M KOH(aq) relative to that of the $p^+$-Si|$NiO_x$ would require the use of a 9.0% efficient Si PV cell with a $V_{oc}$ = 600 mV, a short-circuit current density ($J_{sc}$) of 34.0 mA·cm$^{-2}$, and a fill factor of 0.42 (1, 38). The performance of the PV-biased electrosynthetic photoelectrode was lower than that of the solid-state PV device (39, 40), likely due to nonideality of the back contact in conjunction with additional front-contact resistance in the amorphous Si layer and surface passivation that was partially degraded during the deposition of the $NiO_x$, both of which led to increased recombination (reduced carrier lifetime) at the front and back interfaces as revealed by a time-resolved microwave conductivity measurement (TRMC) (*SI Appendix*, Fig. S7).

Fig. 4*A* shows chronoamperometric data for HTJ-Si|$NiO_x$, n-CdTe|$NiO_x$, and *a*-Si:H|$NiO_x$ photoanodes in contact with 1.0 M KOH(aq) and under simulated 1-Sun illumination. The current density at 1.73 V vs. RHE decreased very slightly over the 100 h of testing for the HTJ-Si|$NiO_x$ photoelectrode, but remained constant for the n-CdTe|$NiO_x$ and *a*-Si:H|$NiO_x$ photoelectrodes. In the absence of protective coatings, these materials showed rapid surface oxidation (*SI Appendix*, Fig. S8 *A–D*) when positively biased under the same conditions, a behavior consistent with the reported anodic oxidation of Si and CdTe in alkaline electrolytes (41, 42). Furthermore, passage of Faradaic current from these bare electrodes under illumination did not yield significant amounts of $O_2$(g) and only effected oxidation of the electrode. In contrast, all of the $NiO_x$-coated electrodes displayed more than 100 h of stability under water-oxidation conditions under simulated 1-Sun illumination in 1.0 M KOH(aq).

Cyclic voltammograms were collected every 10 h during the chronoamperometric stability tests, and Fig. 4*B* shows representative *J-E* data for HTJ-Si|$NiO_x$, n-CdTe|$NiO_x$, and *a*-Si:H|$NiO_x$ photoanodes in contact with 1.0 M KOH(aq) under 100 mW·cm$^{-2}$ of simulated illumination. The photocurrent-onset potentials referenced to $E^{o\prime}(O_2/H_2O)$ were −70 mV and −116 mV and the photocurrent densities at $E^{o\prime}(O_2/H_2O)$ were 5.2 mA·cm$^{-2}$ and 3.3 mA·cm$^{-2}$, for the n-CdTe|$NiO_x$ and *a*-Si:H|$NiO_x$ photoanodes, respectively, under simulated 1-Sun illumination. These values remained unchanged after 100 h. Decreases were observed for the n-CdTe|$NiO_x$ photoelectrode after 1,000 h of continuous operation, where the photocurrent onset potential dropped to −30 mV and the photocurrent density at the equilibrium water-oxidation potential dropped to 1.4 mA·cm$^{-2}$. The Ni(II/III) redox peaks in general increased in current and separated in potential during the stability tests, suggesting an increase in catalytically active sites, loss of reversibility, and/or an increase in resistance.

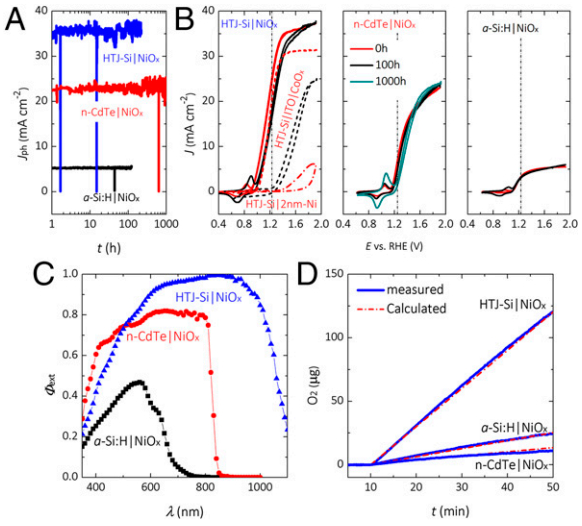


**Fig. 4.** (*A*) Chronoamperometry of HTJ-Si|$NiO_x$, n-CdTe|$NiO_x$, and *a*-Si:H|$NiO_x$ photoelectrodes in contact with 1.0 M KOH(aq) under 100 mW·cm$^{-2}$ of simulated AM 1.5-G solar illumination from an ENH-type tungsten-halogen lamp. The electrodes were maintained potentiostatically at 1.73 V vs. RHE. (*B*) *J-E* data for HTJ-Si|$NiO_x$, n-CdTe|$NiO_x$, and *a*-Si:H|$NiO_x$ photoanodes before and after 100 h of chronoamperometric stability testing in 1.0 M KOH(aq). *J-E* data for n-CdTe|$NiO_x$ after 1,000 h are also included. *J-E* data for an HTJ-Si|ITO|$CoO_x$ photoanode before (red dashed curve) and after a 20-h (black dashed curves) stability test in KOH, as well as for an HTJ-Si|Ni (red dashed-dotted curve) photoanode, are also included for comparison purposes. (*C*) Behavior of the external quantum yield vs. wavelength for HTJ-Si|$NiO_x$, n-CdTe|$NiO_x$, and *a*-Si:H|$NiO_x$ photoelectrodes in 1.0 M KOH(aq). (*D*) Faradaic efficiency for $O_2$(g) evolution at HTJ-Si|$NiO_x$, n-CdTe|$NiO_x$, and *a*-Si:H|$NiO_x$ photoelectrodes under 100 mW·cm$^{-2}$ of AM 1.5-G simulated solar illumination in 1.0 M KOH(aq) with the electrode held at a potential sufficient to maintain a constant current density of 1 mA·cm$^{-2}$ or lower for 40 min. The mass of $O_2$(g) that would be produced by an electrode operating at 100% Faradaic efficiency calculated based on the total charge passed (red dotted lines) and the mass of $O_2$(g) measured experimentally (blue solid lines) using a calibrated $O_2$ probe are shown.

A more significant degradation of the photoanodic performance was observed for the HTJ-Si|$NiO_x$ photoelectrodes, which resulted from a decrease in the photocurrent density at the equilibrium water-oxidation potential from 24.3 $mA{\cdot}cm^{-2}$ to 16.3 $mA{\cdot}cm^{-2}$, whereas a small change (~40 mV anodic shift) was noted in the photocurrent-onset potential after 100 h. The degradation of the HTJ-Si|$NiO_x$ photoelectrodes during 100 h of operation could be caused by oxidation of the thin $p^+$-*a*-Si(6 nm)|i-*a*-Si (5 nm) on c-Si, because this junction is sensitive to the changes caused by oxidation. Oxidation of either of the thin *a*-Si layers can result in a reduction in band bending due to the degraded $p^+$-*a*-Si emitter and/or a reduction in the surface passivation provided by the i-*a*-Si layer.

For comparison, a thin (2 nm) Ni metal-coated HTJ-Si (HTJ-Si|Ni) photoanode showed strong signs of oxidation during the first five cyclic voltammetric scans (dashed-dotted red line in Fig. 4*B*), indicating that the buried junctions were completely destroyed due to anodic Si oxidation, with diode behavior then restored due to the formation of interfacial silicon oxide during subsequent cyclic voltammetric cycles (*SI Appendix*, Fig. S6*B*). For additional comparison, In-doped $SnO_2$ (ITO)-coated HTJ-Si electrodes were coated with electrodeposited Co-Pi (phosphate-containing $CoO_x$, HTJ-Si|ITO|Co-Pi) and characterized electrochemically (*SI Appendix*, *Text S2*, provides a detailed description of characterization methods). A HTJ-Si|ITO|Co-Pi photoanode in 1.0 M KOH(aq) (HTJ-Si|ITO|$CoO_x$ when in alkaline media, *SI Appendix*, Fig. S9) exhibited lower catalytic activity than the $NiO_x$ presented herein and also yielded a continuous degradation in performance during operation. Thus, the ITO/$CoO_x$ films produced a lower solar-to-$O_2$(g) ideal regenerative cell efficiency than that observed for the stable, essentially transparent, protective and highly catalytic $NiO_x$ films reported herein.

Fig. 4*C* shows the wavelength ($\lambda$)-dependent external quantum yield ($\Phi_{ext}$) for HTJ-Si|$NiO_x$, n-CdTe|$NiO_x$, and *a*-Si:H|$NiO_x$ photoelectrodes maintained potentiostatically at 1.93 V vs. RHE, at which the light-limited current density was produced. The quantum yields of the HTJ-Si|$NiO_x$ structure were higher than the values reported for analogous HTJ-Si–based solid-state devices (39). The higher value of $\Phi_{ext}$ can be ascribed primarily to the antireflective behavior and broadband suppression of reflection by the $NiO_x$ film on the textured HTJ-Si surface maintained under working conditions. The decrease in $\Phi_{ext}$ at low and high wavelengths, respectively, was primarily attributable to recombination at the textured front and back interfaces between the crystalline Si and the *a*-Si surface passivation layer (39). The low blue response was also associated with absorption by the *a*-Si heterogeneous coating. The $\Phi_{ext}$ observed for the n-CdTe|$NiO_x$ photoanode is comparable to the behavior reported previously for n-CdTe photoanodes (43). The low $\Phi_{ext}$ values for $\lambda > 500$ nm can be further attributed to the higher reflection (*SI Appendix*, Fig. S4*C*) at these wavelengths. The quantum yield data for the *a*-Si:H|$NiO_x$ photoelectrode were in agreement with previous measurements on *a*-Si:H|$CH_3OH$–1.0 M $LiClO_4$–0.10 mM 1,1′-dimethylferrocene ($Me_2Fe$)–0.0010 mM $Me_2Fe^+$ interfaces (44). The value of $\Phi_{ext}$ for *a*-Si:H can be further improved to match the absorption spectrum to its highest internal quantum yield (typically in the wavelengths of 400–550 nm) by reducing the thickness of $NiO_x$ to an optimum calculated value of 42–53 nm.

Fig. 4*D* shows the Faradaic efficiency for the production of $O_2$(g) by the HTJ-Si|$NiO_x$, n-CdTe|$NiO_x$, and *a*-Si:H|$NiO_x$ photoelectrodes operated for 50 min in 1.0 M KOH(aq) at a bias sufficient to maintain a photocurrent density of 1 $mA{\cdot}cm^{-2}$. The mass of $O_2$(g) that would be produced based on the total charge passed and assuming 100% Faradaic efficiency was in excellent agreement with the measured mass of $O_2$ determined using a calibrated $O_2$ probe. Hence, all three electrodes evolved $O_2$(g) with ~100% Faradaic efficiency under these conditions.

Defects in the sputtered $NiO_x$ films are produced primarily by textures and arcs that are present during sputtering. These defects do not allow complete isolation of the underlying light absorbers from contact with the electrolyte. To demonstrate this behavior, $NiO_x$-coated Si(100) and Si(111) electrodes were immersed for 240 h in 10.0 M KOH(aq). The anisotropic etching of Si(100) was clearly visible and resulted in the formation of inverted pyramid structures (*SI Appendix*, Fig. S10*A*), whereas no significant change in morphology was observed on either Si(111) or $NiO_x$-coated Si(111) surfaces immersed in 10.0 M KOH(aq).

Despite this access to the electrolyte, the $NiO_x$ coatings allowed for the stable, continuous oxidation of water in 1.0 M KOH(aq) for >1200 h on both n-Si(111) and n-Si(100) surfaces (15). A reasonable hypothesis explaining the ability to realize long-term stability using this protection scheme can be based on anodic oxidation of the underlying light absorber by the formation of nondissolvable oxides. During the initial operation of the photoelectrode under anodic bias, $SiO_2$ can be formed on crystalline Si, as well as on the HTJ-Si cell and on the *a*-Si:H surfaces, through pinholes and/or defects in the $NiO_x$ film. Similarly, a passivating layer of $CdTeO_3$ can be formed on CdTe photoanodes (41, 43). After a passivating oxide forms at sites of defects in the $NiO_x$ film, the reaction kinetics for continuous oxide growth are significantly slower relative to those for the oxidation of water by the $NiO_x$ film, and thus oxidation of water then becomes the dominant anodic process. The slow etching rate of these oxides in 1.0 M KOH(aq) is also critical to producing a near-unity Faradaic efficiency for $O_2$(g) evolution.

The ability of the electrocatalytic sputtered $NiO_x$ coating to stabilize the underlying semiconductor under these conditions thus depends on the ability of the photoanode to form a nondissolvable self-passivating oxide. Consistently, a $NiO_x$-coated $n^+$-GaAs photoanode showed a continuously increasing corrosion/dissolution current below the equilibrium water-oxidation potential in 1.0 M KOH(aq) during cyclic voltammetric scans (*SI Appendix*, Fig. S10*B*). Catastrophic surface damage was observed on GaAs (*SI Appendix*, Fig. S10*B*, *Inset*), mainly because of the dissolution of the oxidized film followed by a lifting off of the $NiO_x$.

Protection of photoanodes by use of a coating of $NiO_x$ has the advantage of integrating the transparent conductive catalyst onto planar and textured semiconductors that can form insoluble oxides through the inherent presence of defects in the sputtered catalyst film. In contrast, amorphous $TiO_2$ films deposited by atomic-layer deposition (ALD) that are conformal and pinhole-free can protect corroding materials like GaAs and other Group III–V and Group II–VI semiconductors (45), as well as a high–aspect-ratio Si microwire-array photoanode (46), whereas sputtered $NiO_x$ does not provide conformal films.

In summary, $NiO_x$ films prepared using reactive sputtering are able to protect not only crystalline Si photoelectrodes, but also a HTJ-Si cell, as well as n-CdTe and *a*-Si:H photoanodes, against corrosion or anodic oxidation, while maintaining the performance of the photoanodes during extended operation (>100 h) under water-oxidation conditions in 1.0 M KOH(aq) under simulated 1-Sun illumination. In addition to imparting prolonged stability to the Si photoanodes, the $NiO_x$ coatings also serve as antireflective coatings that increase the amount of light absorbed and thus increase the solar-to-$O_2$(g) ideal regenerative cell efficiency of such electrodes. Optimization of the conditions used to deposit the $NiO_x$ films is critical to obtaining the observed performance of the photoelectrodes, particularly with respect to minimization of the resistivity, maximization of the transparency, and minimization of the electrochromic darkening of the resulting films. This work demonstrates that coatings of p-type transparent conducting oxides can be successfully used to protect a high-efficiency, small-band-gap semiconducting photoanode in a water-splitting device. Hence, $NiO_x$ coatings are a promising approach to the long-term stabilization of self-passivating semiconductors for use in solar-fuels applications. The coating is especially useful for PV-biased electrosynthetic systems that either use or form buried

junctions in situ, but the method is not amenable to materials with active majority-carrier–based grain-boundary shunts such as direct photoelectrochemical cells based on semiconductor/liquid junctions. Improvements in the performance of the in situ Schottky contacts in each case can be expected based on band-edge and interfacial engineering of the energetics at the absorber/protective layer interface. Hence, the sputtered $NiO_x$ protective layer allows a variety of photoanode materials to be considered as options for PV-biased electrosynthetic cells that involve water oxidation in alkaline media, where intrinsically safe, efficient solar-driven electrolysis systems can be constructed (4–6).

## Materials and Methods

The $NiO_x$ films were deposited by reactive radio-frequency sputtering onto substrates under various heating temperatures, using a high-vacuum magnetron sputtering system in a chamber with a maximum base pressure of $8 \times 10^{-8}$ Torr. The $O_2$/Ar ratio was varied from 0 to 0.33 with a constant Ar flow of 20 sccm (standard cubic centimeters per minute) whereas the working pressure was held at 5 mTorr. *SI Appendix, Text S1*, provides details on the preparation of the $p^+$-Si, n-Si, *a*-Si:H, HTJ-Si, n-CdTe, and $n^+$-GaAs substrates and on the sputtering conditions used to grow the $NiO_x$ films. Electrochemical experiments, including measurements of the electrocatalytic performance of the $NiO_x$ films and chronoamperometric stability testing of electrodes, were performed using a three-electrode configuration under potential control with a Hg/HgO/1.0-M KOH reference electrode and a carbon-cloth counter electrode. *SI Appendix, Text S2*, provides details on characterization of electrodes, including stability-measurement protocols, preparation of the HTJ-Si|ITO|Co-Pi photoelectrode, X-ray photoelectron spectroscopy, X-ray diffraction spectroscopy, time-resolved microwave conductivity, spectroscopic ellipsometry, Faradaic efficiency measurements, and total reflectance calculations.

**ACKNOWLEDGMENTS.** This material is based on work performed by the Joint Center for Artificial Photosynthesis, a Department of Energy (DOE) Energy Innovation Hub, supported through the Office of Science of the US DOE under Award DE-SC0004993. N.T.P. acknowledges support from the Graduate Research Fellowship Program of the US National Science Foundation. B.S.B. was supported by the Beckman Institute of the California Institute of Technology. This work was also supported by the Gordon and Betty Moore Foundation under Award GBMF1225.

1. Walter MG, et al. (2010) Solar water splitting cells. *Chem Rev* 110(11):6446–6473.
2. Lewis NS, Nocera DG (2006) Powering the planet: Chemical challenges in solar energy utilization. *Proc Natl Acad Sci USA* 103(43):15729–15735.
3. Hu S, Xiang C, Haussener S, Berger AD, Lewis NS (2013) An analysis of the optimal band gaps of light absorbers in integrated tandem photoelectrochemical water-splitting systems. *Energy Environ Sci* 6:2984–2993.
4. Jin J, et al. (2014) An experimental and modeling/simulation-based evaluation of the efficiency and operational performance characteristics of an integrated, membrane-free, neutral pH solar-driven water-splitting system. *Energy Environ Sci* 7(10):3371–3380.
5. Haussener S, et al. (2012) Modeling, simulation, and design criteria for photoelectrochemical water-splitting systems. *Energy Environ Sci* 5:9922–9935.
6. McKone JR, Gray HB, Lewis NS (2013) Will solar-driven water-splitting devices see the light of day? *Chem Mater* 26(1):407–414.
7. Jia Q, Iwashina K, Kudo A (2012) Facile fabrication of an efficient $BiVO_4$ thin film electrode for water splitting under visible light irradiation. *Proc Natl Acad Sci USA* 109(29):11564–11569.
8. Alibabaei L, et al. (2013) Solar water splitting in a molecular photoelectrochemical cell. *Proc Natl Acad Sci USA* 110(50):20008–20013.
9. Nielander AC, Shaner M, Papadantonakis KM, Francis SA, Lewis NS (2014) A taxonomy for solar fuels generators. *Energy Environ Sci* 8:16–25.
10. Kilby JS, Lathrop JW, Porter WA (1977) Solar energy conversion. *US Patent* 4,021,323.
11. Rocheleau RE, Miller EL, Misra A (1998) High-efficiency photoelectrochemical hydrogen production using multijunction amorphous silicon photoelectrodes. *Energy Fuels* 12(1):3–10.
12. Ayers W (1984) Photolytic production of hydrogen. *US Patent Application* 06/523,251.
13. Reece SY, et al. (2011) Wireless solar water splitting using silicon-based semiconductors and earth-abundant catalysts. *Science* 334(6056):645–648.
14. Sun K, et al. (2014) Enabling silicon for solar-fuel production. *Chem Rev* 114(17):8662–8719.
15. Sun K, et al. (2015) Stable solar-driven water oxidation to $O_2$(g) by Ni-oxide coated silicon photoanodes. *J Phys Chem Lett* 6:592–598.
16. Mei B, et al. (2014) Iron-Treated NiO as a Highly Transparent p-Type Protection Layer for Efficient Si-Based Photoanodes. *J Phys Chem Lett* 5(20):3456–3461.
17. Hunter BM, et al. (2014) Highly active mixed-metal nanosheet water oxidation catalysts made by pulsed-laser ablation in liquids. *J Am Chem Soc* 136(38):13118–13121.
18. Smith RDL, et al. (2013) Photochemical route for accessing amorphous metal oxide materials for water oxidation catalysis. *Science* 340(6128):60–63.
19. Miller EL, Rocheleau RE (1997) Electrochemical and electrochromic behavior of reactively sputtered nickel oxide. *J Electrochem Soc* 144(6):1995–2003.
20. Trotochaud L, Young SL, Ranney JK, Boettcher SW (2014) Nickel-iron oxyhydroxide oxygen-evolution electrocatalysts: The role of intentional and incidental iron incorporation. *J Am Chem Soc* 136(18):6744–6753.
21. Friebel D, et al. (2015) Identification of highly active Fe sites in (Ni,Fe)OOH for electrocatalytic water splitting. *J Am Chem Soc* 137(3):1305–1313.
22. Alsabet M, Grdeń M, Jerkiewicz G (2014) Electrochemical growth of surface oxides on nickel. Part 3: Formation of β-NiOOH in relation to the polarization potential, polarization time, and temperature. *Electrocatalysis* 6(1):60–71.
23. Bode H, Dehmelt K, Witte J (1966) Contribution to the Knowledge of Nickel Hydroxide Electrodes 1. About The Nickel(II) Hydroxide Hydrate. *Electrochim Acta* 11(8):1079–1087.
24. Louie MW, Bell AT (2013) An investigation of thin-film Ni-Fe oxide catalysts for the electrochemical evolution of oxygen. *J Am Chem Soc* 135(33):12329–12337.
25. Guzmán RSS, Vilche JR, Arvía AJ (1979) Non-equilibrium effects in the nickel hydroxide electrode. *J Appl Electrochem* 9(2):183–189.
26. Xing W, Li F, Yan Z-f, Lu GQ (2004) Synthesis and electrochemical properties of mesoporous nickel oxide. *J Power Sources* 134(2):324–330.
27. Tuomi D (1965) The forming process in nickel positive electrodes. *J Electrochem Soc* 112(1):1–12.
28. Herzinger CM, Johs B, McGahan WA, Woollam JA, Paulson W (1998) Ellipsometric determination of optical constants for silicon and thermally grown silicon dioxide via a multi-sample, multi-wavelength, multi-angle investigation. *J Appl Phys* 83(6):3323–3336.
29. Woollam JA, McGahan WA, Johs BD (1994) Ellipsometric measurement of the optical properties and electrical conductivity of indium tin oxide thin films. Optical interference coatings. *Proc SPIE* 2253:962–968.
30. Petrov I, Barna PB, Hultman L, Greene JE (2003) Microstructural evolution during film growth. *J Vac Sci Technol A* 21(5):S117–S128.
31. Trotochaud L, Mills TJ, Boettcher SW (2013) An optocatalytic model for semiconductor–catalyst water-splitting photoelectrodes based on in situ optical measurements on operational catalysts. *J Phys Chem Lett* 4(6):931–935.
32. Granqvist CG (1995) Preface. *Handbook of Inorganic Electrochromic Materials*, ed Granqvist CG (Elsevier, Amsterdam), pp vii–viii.
33. Hackwood S, Dautremont-Smith WC, Beni G, Schiavone LM, Shay JL (1981) Volume changes induced by the electrochromic process in sputtered iridium oxide films. *J Electrochem Soc* 128(6):1212–1214.
34. Andersson AM, Estrada W, Granqvist C-G, Gorenstein A, Decker F (1990) Characterization of electrochromic dc-sputtered nickel-oxide-based films. Optical materials technology for energy efficiency and solar energy conversion IX. *Proc SPIE* 1272:96–110.
35. Korošec RC, Bukovec P (2006) Sol–gel prepared NiO thin films for electrochromic applications. *Acta Chim Slov* 53:136–147.
36. Wronkowska AA (1989) An ellipsometric investigation of nickel oxide films in alkaline solution: The multilayer film approach. *Surf Sci* 214(3):507–522.
37. Ord JL (1976) An optical study of the deposition and conversion of nickel hydroxide films. *Surf Sci* 56(0):413–424.
38. Mills TJ, Lin F, Boettcher SW (2014) Theory and simulations of electrocatalyst-coated semiconductor electrodes for solar water splitting. *Phys Rev Lett* 112(14):148304.
39. Wang H-P, et al. (2013) Realizing high-efficiency omnidirectional n-type Si solar cells via the hierarchical architecture concept with radial junctions. *ACS Nano* 7(10):9325–9335.
40. Taguchi M, et al. (2014) 24.7% record efficiency HIT solar cell on thin silicon wafer. *IEEE J Photovoltaics* 4(1):96–99.
41. Ahearn JS, Davis GD, Byer NE (1982) Mechanism of anodic oxidation of $Hg_{0.8}Cd_{0.2}Te$. *J Vac Sci Technol* 20(3):756–759.
42. Philipsen HGG, Kelly JJ (2005) Anisotropy in the anodic oxidation of silicon in KOH solution. *J Phys Chem B* 109(36):17245–17253.
43. Lichterman MF, et al. (2014) Stabilization of n-cadmium telluride photoanodes for water oxidation to $O_2$(g) in aqueous alkaline electrolytes using amorphous $TiO_2$ films formed by atomic-layer deposition. *Energy Environ Sci* 7:3334–3337.
44. Kumar A, Lewis NS (1990) Short-wavelength spectral response properties of semiconductor/liquid junctions. *J Phys Chem* 94(15):6002–6009.
45. Hu S, et al. (2014) Amorphous $TiO_2$ coatings stabilize Si, GaAs, and GaP photoanodes for efficient water oxidation. *Science* 344(6187):1005–1009.
46. Shaner MR, Hu S, Sun K, Lewis NS (2015) Stabilization of Si microwire arrays for solar-driven $H_2O$ oxidation to $O_2$(g) in 1.0 M KOH(aq) using conformal coatings of amorphous $TiO_2$. *Energy Environ Sci* 8:203–207.